

Structural origins of the cohesive energy in metal-terpyridine oligomer thin-films†

Velimir Meded,^{*a} Nikolaus Knorr,^b Tobias Neumann,^a Gabriele Nelles,^b Wolfgang Wenzel^a and Florian von Wrochem^{id} ^{*b}

Fe^{II}-terpyridine based oligomers have attracted considerable interest as key constituents for the realization of highly robust, ultra-thin ordered layers of metal center oligomers (MCOs) for organic electronics applications. By using molecular simulations and nanotribology investigations, we report on the origins of the surprisingly high mechanical and thermal stability in this type of MCO layers, which finds its expression in nanowear resistance values of up to 1.5 μN for the MCO films, as well as in a thermal stability of two-terminal MCO junctions to temperatures up to ~ 100 °C under electrical load. A theoretical analysis of the fundamental cohesive forces among the constituents within the context of an electrostatic model reveal that the cohesive energy is essentially based on Coulomb interactions among the ionic constituents of the oligomers, leading to an estimated cohesive energy per molar mass of 0.0132 eV mol g⁻¹ for MCO layers that advantageously compare to the 0.0061 eV mol g⁻¹ reported for pentacene crystals.

Despite the recent progress in materials research, the realization of robust molecular devices based on single ultrathin molecular layers of a few nanometers thickness is still a tremendous challenge. In part, this is attributed to the possible nanoscale-defects and grain boundaries within the organic layer that compromise device operation (particularly in macroscopic junctions with up to 10^4 μm^2 active device area). But more significantly, the high-temperature deposition of the electrode by physical vapour deposition represents a real challenge, as it usually damages the highly vulnerable functional molecular layers.^{1,2} In order to overcome these hurdles, and to finally achieve an extension of lifetime and temperature stability of thin-film molecular devices, a number of strategies have been envisioned in recent years. They range from the protection of ultrathin functional layers by intermediate polymeric,³ graphene,⁴ or inorganic^{5,6} layers, over a more robust coordination of the organic layers to the substrate,^{7,8} to the enhancement of the intrinsic film stability by enforcing the intramolecular interactions, an approach recently endeavored in our laboratory for the formation of molecular junctions based on ultrathin metal-terpyridine complex oligomers.^{9,10}

Metal-terpyridine redox complexes^{11,12} are promising systems for organic and molecular electronics applications, as their

terpyridine ligands are versatile building blocks allowing for complexation of a variety of metal transition metal cations.¹³ This enables the vertical control of both junction-thickness and -architecture within a layer by layer (LbL) deposition process of metal ions and complexing terpyridine ligands.^{11,14} Electron transfer along metal-terpyridine molecular wires has been investigated by electrochemical means,¹⁵ with liquid electrodes,¹⁰ by scanning probe methods,¹⁶ or with intermediate polymeric layers.¹⁷ We have recently demonstrated the outstanding mechanical and electrical robustness that can be achieved by large-area junctions of terpyridine-based metal-organic complex oligomers (herein defined as metal center oligomers (MCOs)).⁹ Indeed, ultrathin (15–30 nm thick) MCO layers were shown to resist direct metal deposition, forming molecular junctions with surprising temperature stability and very long operational lifetimes.

In this paper, the nano-mechanical properties and the cohesive energy of MCO layers are studied by atomic force microscopy and periodic atomistic simulations, respectively. From the analysis of the wear curves we deduce a high mechanical stability, and molecular simulations show evidence of higher cohesive energy densities than known from typical van der Waals solids, which is attributed to the strong quasi-periodic electrostatic interactions among Fe^{II}-cations and triflate (NH₄CF₃SO₃) anions, as well to the relative order in the dense, quasi-crystalline MCO films. From a very fundamental point of view, higher cohesive energies explain the higher temperature stability, as the barriers to access other configurations in conformational phase space are raised.

^a Institute of Nanotechnology, Karlsruhe Institute of Technology, 76021 Karlsruhe, Germany. E mail: velimir.meded@kit.edu

^b Materials Science Laboratory, Sony Europe Ltd, Zn Deutschland, Hedelfinger Strasse 61, 70327 Stuttgart, Germany. E mail: Florian.vonWrochem@eu.sony.com

† Electronic supplementary information (ESI) available: Details on chemicals, AFM data, and model structure generation. See DOI: 10.1039/c7cp05488b

Mechanical stability from nano-wear measurements

Since the development of scanning probe methods, nano-mechanical measurements to quantify the frictional response of inorganic and organic layers (*e.g.* polymers) emerged as a valid tool for monitoring the mechanical stability and tribological properties of these layers at the nanoscale. Although indirect, these types of measurements allow drawing a correlation between mechanical film robustness (hardness of the material) and the cohesive energy among the molecular units (in this case the MCO monomers).¹⁸ In the present study, cohesive energies are modelled by atomistic simulations (*vide infra*), revealing the interaction forces by which MCO layers exhibit such an extraordinary mechanical stability as has been recently demonstrated.⁹

The substrate for the preparation of the MCO films is given by Au electrodes that are thermally evaporated on silicon substrates. For a reliable attachment of the MCO layer to these Au electrodes, a seed layer formed by the co-deposition of 4'-(4-mercaptophenyl)-terpyridine (MPTP) with mercaptobenzene on Au is initially required.¹⁹ Then, the oligomers are assembled by a stepwise sequential coordination reaction of a Fe^{II} redox center with a conjugated 1,4-di(2';6';2''-terpyridine-4'-yl)benzene (TPT) ligand (see Fig. 1a and Methods section), as previously described⁹ and as summarized in the Methods section. Here, oligomers of two different lengths have been grown by the stepwise sequential deposition of 20 and 30 Fe^{II} MCs, yielding MCO layers with a thickness of 20 and 30 nm, respectively.

A constant increment in film thickness as a function of the coordination number is deduced from atomic force microscopy (AFM) topographic scans, resulting in a value of ~ 1.08 nm per coordination step (Fig. S1, ESI[†]). This is in line with the coordination efficiency already known from previous works,¹⁹ where a self-limiting layer-by-layer build-up have been demonstrated.²⁰

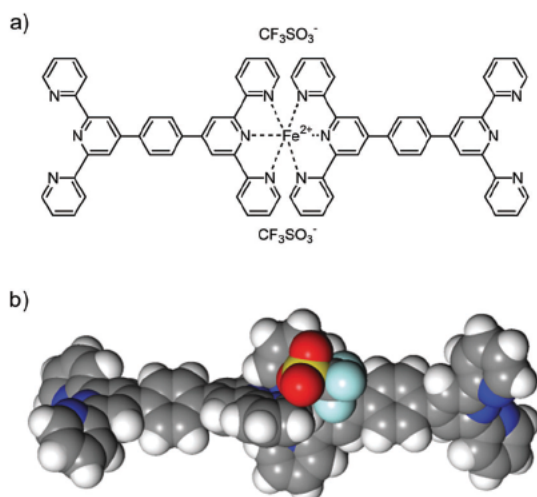


Fig. 1 (a) Chemical structure of a single 1,4-di(2';6';2''-terpyridine-4'-yl)benzene (TPT) dimer. (b) 3D model of the dimer from a gas phase geometry optimization by density functional theory (DFT) calculations (see Methods section). Color code: carbon (grey), nitrogen (blue), oxygen (red), fluorine (marine), sulphur (yellow), iron (magenta).

Based on the repeat unit length of the TPT unit as computed by DFT calculations⁹ and based on the MCO layer thickness as obtained from AFM data (Fig. S1, ESI[†]), an orientation of the oligomer backbone at an angle of $\sim 46^\circ$ from the surface normal is deduced. This is also concluded from the circumstance that the metal-bisterpyridine complex assumes an octahedral geometry with limited bending degrees of freedom, thus that the MCO oligomer can be considered as a linear chain, so the dependence of film thickness on the number of deposition cycles is a direct indicator of the molecular chain inclination. Furthermore, the same chain orientation has been independently obtained from atomistic simulations in our previous work on charge transport in MCO layers.⁹

The mechanical stability of the films is determined by AFM-based nanowear measurements. For this scope, three different types of samples were compared, *i.e.* MCO films with 20 and 30 MCs (deposition cycles), as well as a poly(methyl methacrylate) (PMMA) film with a thickness of 35 nm, used as a reference system. Scratching experiments are performed with a range of probe loads (from 40 nN to 2 μ N) on a surface area of $2 \times 2 \mu\text{m}^2$ in order to monitor the dependence of the wear on the applied load. For this aim, a single scan is first done in contact mode with a controlled constant probe load force, using scan parameters as specified in the Methods section. Subsequently, as a measure of sample wear, the average AFM topographic height h of the central region ($1 \times 1 \mu\text{m}^2$) of the scratched area ($2 \times 2 \mu\text{m}^2$) relative to the average height of the unscratched area has been determined. The wear patterns as a function of loads on the AFM probe are shown in AFM topographic images recorded over a $5 \times 5 \mu\text{m}^2$ area, in which the square pattern of the previously scratched area is enclosed (Fig. 2). As a reference, a 35 nm thick PMMA polymer layer was scratched under analogous conditions, as shown in Fig. 3. The surface scans presented in Fig. 2 and 3 are just a selection of scans from the full body of our data (see Fig. 4). The full sequence of AFM surface scans for the other probe loads is shown in Fig. S2 (ESI[†]). PMMA is used as a reference material because grafted PMMA layers are known to be quite robust against nanowear treatment.²¹

We observe a pronounced wear resistance of the MCO layer for all loads below 500 nN. Neither the nanoscale roughness nor the average height of the film is significantly affected by the nanowear scans (Fig. 2b). For higher loads (Fig. 2c and d), the thickness of the MCO layer is reduced more or less proportionally to the applied load, until a maximum of $\Delta h = 8$ nm for a load of 2 μ N has been reached. At higher loads, irregular disruptive abrasion of the films sets in, resulting in the removal of parts of the TPT oligomers from the Au substrate (not shown). As a reference, we performed an analogous series of scans with a 35 nm thick PMMA polymer layer, whose nanomechanical properties are already known from literature.^{21–23} Under the same scan conditions, PMMA layers show evidence of plastic deformation due to viscoelastic relaxation of the polymer matrix, which sets in already at moderate applied scan loads. Specifically, above 200 nN, the formation of characteristic ripple patterns begins, that gradually increase as the load is enhanced (see Fig. 3). This is in line with an earlier report from Berger *et al.*, who reported

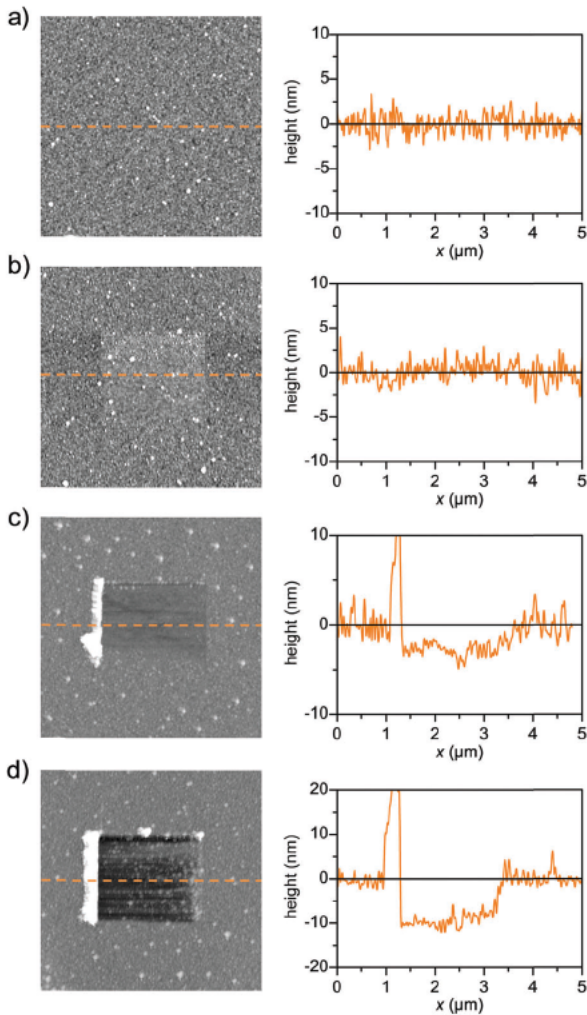


Fig. 2 Topographic AFM surface scans ($5 \mu\text{m} \times 5 \mu\text{m}$, left) and horizontal center line cuts of the MCO 20 layer (right) of the pristine surface (a) and of a $2 \mu\text{m} \times 2 \mu\text{m}$ area that has been treated by nanowear with applied loads of 400 nN (b), 800 nN (c) and $2 \mu\text{N}$ (d); grayscales: $\pm 5 \text{ nm}$ (a) and $\pm 15 \text{ nm}$ (b and c).

that rippling in PMMA layers is barely observed below a wear load of 40 nN.²¹ The ripples are attributed to the very slow relaxation dynamics of the polymer network, as the polymer chains displaced by the mechanical action of the cantilever are not immediately equilibrated to their original location, essentially due to viscous dissipation processes.^{24,25} In parallel with this viscoelastic deformation, we observe that for scans with a load from 150 nN to $0.8 \mu\text{N}$, the mean height of the worn region is augmented over that of the unaltered surroundings (see section in Fig. 3a and b), which is indicative of scan-induced crazing and consequent void formation within the PMMA layer (volume expansion).^{21,24}

Note that whereas for MCO films minor fractions of the layer are removed comparatively homogeneously at higher loads, in PMMA films wear initially results in a roughening and rippling of the surface (below $0.8 \mu\text{N}$), followed by an abrupt removal of the whole polymer film at $\sim 1.5 \mu\text{N}$. Fig. 4 summarizes for MCO and PMMA layers the dependency of the average height on the

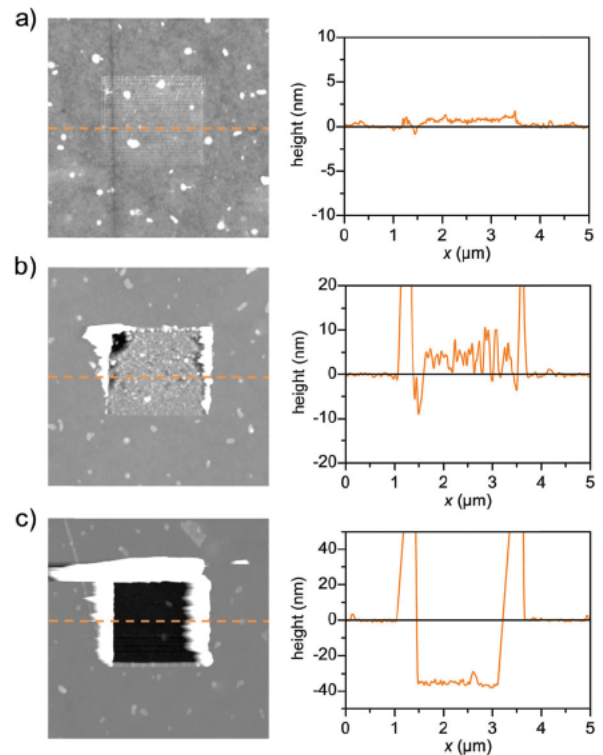


Fig. 3 Topographic AFM surface scans ($5 \mu\text{m} \times 5 \mu\text{m}$, left) and horizontal center line cuts of a $2 \mu\text{m} \times 2 \mu\text{m}$ worn area within the PMMA layer (right), that has been treated with an applied load of 240 nN (a), 600 nN (b) and $1.4 \mu\text{N}$ (c); grayscales: $\pm 5 \text{ nm}$ (a); $\pm 20 \text{ nm}$ (b); and $\pm 40 \text{ nm}$ (c). At low loads, a rippling of the polymer film along with an increased average height in the scratched region is observed (a and b). At loads above 800 nN, disruptive changes are observed, resulting in the complete removal of the PMMA layer.

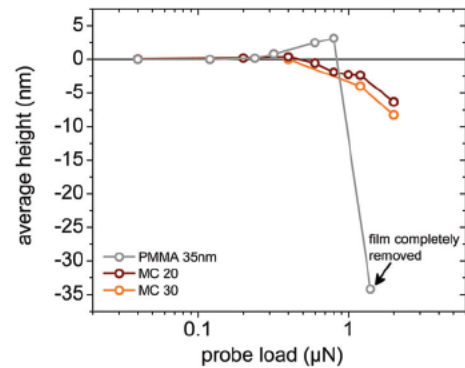


Fig. 4 Average height of the central $1 \mu\text{m}^2$ region within the scratched ($2 \mu\text{m} \times 2 \mu\text{m}$) area, relative to the height of the surrounding pristine layer (see Fig. 2 and 3), plotted against the applied probe load during nanowear.

applied probe loads. In the figure, also the wear behavior of two MCO layers with 20 and 30 deposition cycles is compared, where the wear resistance for both layers matches almost perfectly. This result is intuitively understandable, considering that the MCO film structure, the cohesive energy, as well as the surface roughness are nearly identical in both cases. The force-dependent changes in the average height indicate a high structural and mechanical stability of MCO layers as referred

to PMMA layers, whose robustness against nanowear treatment has already been reported earlier.²¹ As a concluding remark, it should be emphasized that besides the cohesive energy also surface roughness plays a role in nanowear resistance, but that this aspect could not be studied in detail within the present work, as no experimental strategies were available to equalize the roughness of polymer layers and MCO surfaces. We have investigated the physical origins of the enhanced stability of MCO thin films by molecular and electrostatic simulations, and the results are presented in the next sections.

Thermal stability

The mechanical stability of the MCO films should go hand in hand with the thermal stability in molecular junctions. We monitored the electrical stability of MCO layers when sandwiched between evaporated Au electrodes in a crossbar geometry, particularly in view of electrical breakdown (short circuit). As previously shown, the sturdiness of organic layers based on Fe^{II}-terpyridine oligomers enables the fabrication of robust, large area junctions for organic electronic applications.⁹ Besides the low defect density of the MCO layers found in such junctions, which allows the realization of two-terminal junctions with areas of over 100 $\mu\text{m} \times 100 \mu\text{m}$, also operational lifetimes of more than 2 years (under applied bias voltages of up to 3 V) could be achieved and, importantly, a remarkable temperature stability either. This is shown in Fig. 5, where current densities J from MCO junctions with 20 and 30 Fe^{II} MCs are displayed. Reproducible currents were measured in a range of temperatures from 98 °C to +94 °C without shorts in the device, a remarkable result considering the small layer thickness (20–30 nm thickness) and the ductile nature of the gold electrodes, which are known to easily form filaments for most organic thin films. Besides the high cohesive energy per molar mass among MCO monomers (as outlined in the theory section further below), only a small defect density in terms of domain boundaries and pinholes can explain our present experimental data.

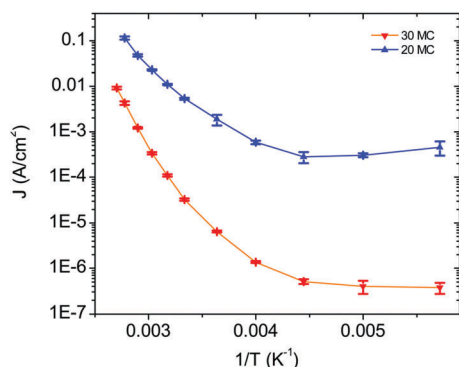


Fig. 5 Temperature dependent J T data for MCO junctions with 20 and 30 MC monomers recorded in the temperature range from 175–367 K (98 °C to 94 °C) under HV conditions (base pressure: 10^{-6} mbar). Current density values (J) are acquired at a bias voltage of 3 V. Experimental details are found in ref. 9.

Simulations for cohesive energy determination

Cohesive energy calculations of a material in the solid state can be correlated with the energetic stability of the phase. In the past, both force field based²⁶ and density functional theory (DFT) methods^{27–29} were used to estimate the energetic phase stability for molecular crystals. In the following we use a combination of the methods to obtain estimates for the cohesive energy.

To estimate energetic phase stability on the basis of DFT calculations we start with the structure as obtained in atomistic Monte Carlo simulations used in our previous work,⁹ displayed in Fig. 6b. The figure illustrates a cut of three oligomers, each five monomers long. Due to the missing periodicity, confirmed by the lack of diffraction reflexes from GIXD experiments,⁹ the simulations reported in ref. 9 did not converge to an atomically precise periodic structure, which substantially limits the possibility of computing cohesive energies in periodic DFT models. We have therefore performed single point electronic structure calculations utilizing the TURBOMOLE computational chemistry code package³⁰ for a finite cluster system. As the large size of the system confined the choice of the basis set and the functional, the def2-SVP³¹ basis set and a pure GGA exchange–correlation functional (BP86^{32,33}) was used. To account for the van der Waals type interactions, empirical Grimme corrections³⁴ were included.

Using this approach we computed the cohesive energy of the finite cluster to 0.31 eV per monomer without dispersive corrections and 0.65 eV with dispersion corrections,³⁴ see columns two and three in Table 1.

Because the system carries high local charges, long range electrostatic effects can be expected to strongly contribute to the cohesive energy. In order to account for these effects we

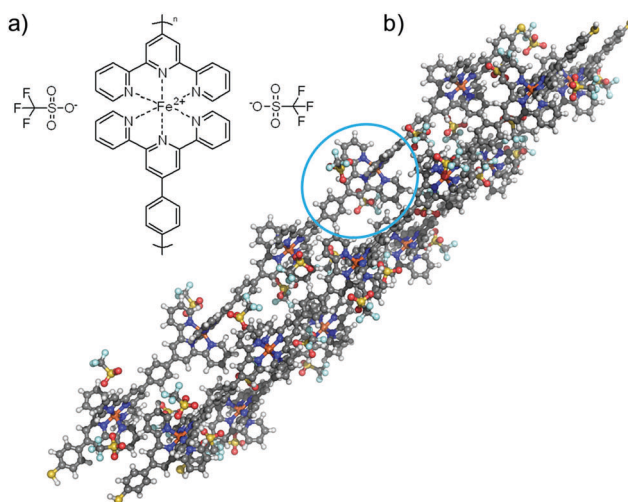


Fig. 6 (a) Chemical structure of the Fe^{II} terpyridine monomer along with the corresponding triflate counter ions (CF₃SO₃⁻) used during the deposition of the MCO layers. (b) 3D model of the three oligomer system used in single point DFT calculations of the MCOs in the bulk phase (b). Each MCO is five monomers long (the blue circle includes a single monomer).

Table 1 Calculated energy differences between interacting and single oligomer systems. The DFT calculations are performed both with and without van der Waals corrections.³⁴ In the electrostatic model (ESM) we calculate the energy for both finite and periodic systems. For the periodic systems we present both energies involving separation of the oligomers with the counter ions attached and the cohesive energies where all inter molecular bonds are broken. All the values are per monomer unit

MCO wire	3 Oligomer no vdW	3 Oligomer with vdW	Periodic	Full cohesive eng.
DFT	0.31 eV	0.65 eV		
ESM	0.25 eV		2.71 eV	10.98 eV

constructed a point charge model taking into account only the Fe^{II}-ions and the counter-ions, based on the atomistic simulations reported in ref. 9. The Fe-centers carry a charge $+2|e|$, while the counter ions carry a charge of $-1|e|$, which represents the electrostatic contribution to the cohesive energy. Obviously, this approach would be valid for any kind of counter ion as long as it shows the same electrostatic properties (namely, its total charge has to be $-1|e|$). The cohesive energy of this periodic array of charges corresponds to the leading monopole contribution of the electrostatic energy of the system. This reduced structural model is based on the finite size atomistic simulations as reported in the above model, but the structure has been periodically extended as the morphology suggested the existence of MCO structures that are periodic in the xy -plane. Based on the atomistic model,⁹ the point charge model for a single wire was constructed by placing n positive charges $q = +2|e|$ at positions

$$(0.0, 0.0, 0.0) + n \times \mathbf{v}_2$$

where n is the number of Fe^{II} centers in a single wire unit, *i.e.* the number of layers. The single-wire point charge model is then extended into a periodic structure by applying periodic boundary conditions with box vectors \mathbf{v}_0 and \mathbf{v}_1 . All reduced unit vectors \mathbf{v}_0 , \mathbf{v}_1 and \mathbf{v}_2 are extracted from the atomistic simulations in ref. 9 and given in the Methods section.

For each redox center, two counter-ions were placed in the middle between the Fe^{II}-ions of two neighboring oligomers. Further details on the oligomer structure definition can be found in the Methods section. A single layer of the periodic point charge model is illustrated in Fig. 7a, while three-dimensional representation for the case of $n = 10$ layers is displayed in Fig. 7b.

While the position of the iron centers and MCOs is determined by the model, the exact position of the counter-ions is not uniquely determined in the simulations we used to construct the model. In order to compute the sensitivity of the total energy to the position of the counter-ions, we perturbed the position of each counter ion independently in many simulations from their initial positions in random directions. The displacement was drawn from a uniform-random distribution with maximal value Δx_{\max} for different values of $\Delta x_{\max} = 0.05$ nm, 0.1 nm, 0.2 nm, and 0.3 nm. The system was sampled using 10^4 MC steps and the energy averaged throughout the run to give an estimate of the dependence of the electrostatic energy on the counter-ion position. As indicated in Fig. S3 (ESI[†]), this

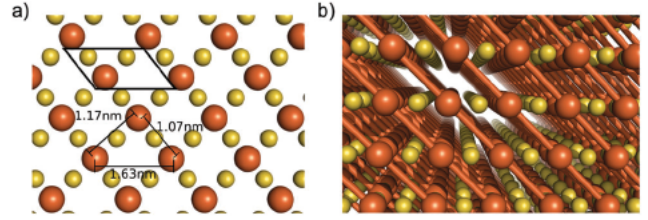


Fig. 7 (a) Single layer of the periodic point charge model. Fe^{II} redox centers (red) are substituted by point charges $q = +2$, the counter ions (yellow) by $q = -1|e|$. The distances between the Fe^{II} redox centers of neighboring wires were extracted from the atomistic model [cite Wires1] and used to calculate the 2D $x y$ periodic unit cell (black rhombus). (b) A 3D model consisting of point charges constructed by a different number of layers n , *i.e.* different lengths of the MCMWs (in the figure: $n = 10$). Fe^{II} redox centers (red) are interspaced by Fe^{II} and counter ions to form a tightly packed cohesive mesh with alternating charges of $+2$ and $-1|e|$, where e is elementary charge. Fe^{II} redox centers of a single MCMW are connected with stick representation for illustration.

variation is modest, due to the long-range nature of the interactions. While the local interaction energy with the nearest ions may change significantly, the total energy is dominated by the long-range contribution of the Ewald sum, which is much less sensitive to either position or chemical nature of the counter ion.

To obtain the cohesive energy of the system, the Coulomb energy was calculated for different numbers of monomers, or length of the oligomers ($n = 3, 5, 10, 15$ and 20) and position of the counter ions using the particle-mesh Ewald summation as implemented in the OpenMM package.^{35,36} In order to compare with the DFT calculations, we also computed the electrostatic cohesive energy of a model corresponding to the units in the DFT cluster calculations reported above.

Direct comparison between the electrostatic model (in which the three oligomers are represented by the charged species only) and the DFT calculations is displayed in Table 1. The energy difference between the three aggregated oligomer- and three single oligomer-calculations was 0.25 eV in the electrostatic model (ESM), which compares well to the 0.31 eV resulting from DFT. The ESM result is clearly of the same order of magnitude as the van der Waals (vdW)-corrected calculation (0.65 eV), indicating that the electrostatic contributions are relevant. The differences between the DFT and the EMS result can arise from the existence of a delocalized charge distribution, which can modify the short-range Coulomb interactions and it is not captured well by EMS. When full periodicity in xy -plane is applied in the electrostatic model, the energy difference is computed as 2.71 eV per monomer. This indicates that the long range contribution to the electrostatic energy is much larger than the short range contribution, as expected by the nature of the Ewald sum. When the cohesive energy, where all ionic inter-molecular bonds (*i.e.* all bonds among Fe^{II} and counter ions) are broken is calculated, we obtain a cohesive energy of 10.98 eV per monomer. We conclude that MCO cohesive energy is comparable to the NaCl crystal, where the experimental cohesive energy of Na⁺ and Cl⁻ amount to 6.8 eV,³⁷ which is considerably larger than the cohesive energy of 1.7 eV per molecule found in pentacene (van der Waals-type) crystals,³⁸ see the first row of Table 2.

Table 2 Comparison of the calculated MCO cohesive energy with literature values for NaCl³⁷ and pentacene.³⁸ The energy values are calculated per monomer and, due to large size discrepancy of the unit cells, per molar mass, or g mol⁻¹

	Per unit cell	Per g mol ⁻¹
MCO	10.98 eV	0.0132 eV
NaCl ³⁷	6.8 eV	0.118 eV
Pentacene ³⁸	1.7 eV	0.0061 eV

The fact that the cohesive energy for MCO is larger than NaCl can be understood in terms of the presence of four charges in the MCO unit *vs.* only two charges in the NaCl unit.

As the difference in unit cell size of MCO (the MCO unit cell is presented in Fig. 6a), NaCl, and pentacene is considerable, the cohesive energies per unit cell may not give a clear picture of energetic stability. Thus, we divide the cohesive energies by the corresponding molar masses. The resulting cohesive energies per molar mass are for NaCl 0.118 eV mol⁻¹, for MCO 0.0132 eV mol⁻¹, and for pentacene 0.0061 eV mol⁻¹ (see the second row in Table 2). These results indicate that MCO oligomers are more stable than pentacene crystals, but not as stable as NaCl crystals. We attribute the difference to larger distances between charges in the MCO system compared to NaCl, as well as to the absence of charge monopoles in pentacene crystals.

Conclusions

We have investigated MCO (Fe^{II}-terpyridine oligomer) layers by nanowear experiments as well as by molecular simulations to reveal the origins for the remarkable mechanical and thermal stability that such layers exhibited in previous studies. By nanowear, we show that a significant abrasion sets in only at cantilever forces above 1500 nN, *i.e.* well above the force for the disruption of PMMA polymer layers. The robustness of MCO layers is rationalized in terms of strong electrostatic interactions acting between the ionic species in the (almost periodic) lattice, which by means of an electrostatic model were shown to stabilize the MCO ionic crystal. Indeed, our estimate yields a cohesive energy per molar mass of 0.0132 eV for the MCO layer, significantly higher than the 0.0061 eV reported for pentacene crystals. This explains why ultrathin MCO layers have been demonstrated to be robust towards direct metal evaporation, forming molecular junctions that exhibit lifetimes of several years.

Methods

Preparation

For the MCO samples, bottom electrodes are realized by the evaporation of 50 nm Au on 5 nm Cr on a Si wafer with 400 nm thermal oxide (sample dimensions: 10 mm × 10 mm), employing an evaporation rate of 0.3 nm s⁻¹. The vapour-deposited gold electrodes are functionalized with a mixed SAM of MPTP/MB (MPTP = 4'-(4-mercaptophenyl)terpyridine, MB = mercaptobenzene), prepared by immersing the electrodes in a degassed equimolar

solution (Note 34 in ref. 39) of MPTP and MB (5×10^{-5} M each, chloroform, 1 day) and by rinsing them with chloroform. The oligomer films are assembled by a stepwise sequential coordination reaction of a Fe^{II} redox center by a conjugated 1,4-di(2;2';6';2''-terpyridine-4'-yl)benzene (TPT) ligand. For this scope, the functionalized substrates are (1) immersed in a solution of Fe(CF₃SO₃)₂ (5×10^{-5} M, ethanol:chloroform 1:1, 5 min) and rinsed with ethanol and chloroform, (2) immersed in a TPT solution (TPT = 1,4-di(2;2';6';2''-terpyridine-4'-yl)benzene, 5×10^{-4} M, chloroform, 20 min) and rinsed with chloroform and ethanol. Stages (1 and 2) are repeated iteratively, whereby the Fe^{II} charges of the metal centers are balanced by triflate counter-ions. Once the desired length is reached, the MCO functionalized gold electrodes are immersed in a MPTP solution (5×10^{-4} M, chloroform, 20 min) and rinsed with chloroform. In our study, two different types of samples were employed, *i.e.* MCO films with a total of 20 and 30 MCs (and TPT monomers). For comparison with the MCO layers, atactic PMMA ($T_g = 105$ °C) with molecular mass of 350 000 g mol⁻¹ was used as received from Polyscience Inc. The PMMA polymer films were deposited by spin-coating from dichlorobenzene solution (1 wt% PMMA, 1000 rotations per minute) on an evaporated Pt film on glass (100 nm thickness).

AFM film thickness measurements of MCO samples

Atomic force microscopy (AFM) scans for film thickness evaluation are performed with a Multimode Nanoscope IIIa (Digital Instruments) on bottom electrode structures, yielding an increment in MCO layer thickness by 1.08 nm per coordination number as shown in Fig. S1 (ESI†).

Nanowear

Nanowear measurements are done using an AFM (Model MFP-3D-TM from Asylum Research). Scratching and topographic imaging are carried out using Si AFM chips from Olympus (Model OMCL AC160TS-W2) with a spring constant of 42 N m⁻¹. AFM data visualization and analysis are carried out using the Gwyddion software tool (Version 2.37). Scratching is performed at probe loads ranging from 40 nN to 2 μN on a surface area of 2 × 2 μm². The scans are executed in contact mode with a controlled constant probe load force (measured *via* the deflection voltage), whereby 64 alternating lines are scanned in both scan directions (forward and backward) at a scan angle of 90° (perpendicular to shaft direction). The scanning speed is 1 μm s⁻¹, whereas the feed-back gain is set to a value of 15. After scratching, topographic scans are recorded in the tapping mode on an area of 5 × 5 μm², encompassing the scratched 2 × 2 μm² surface area in the center of the micrograph.

Simulations

As the Fe^{II}-centers are essentially +2 charged ions, and the counter-ions are -1 charged molecules, placed in proximity to the Fe-centers, the simplest estimate of the electrostatic interactions, taking only the leading contributions into account, is achieved by representing the positively charged Fe-centers simply by point charges (with charge +2) same as the corresponding counter-ions (with charge -1).

We use periodic box vectors in xy -plane, extracted from atomistic calculations (ref. 9, see ESI† for the details on MCO structure simulations) and transformed into reduced unit cell vectors, given as

$$\nu_0 = (1.211 \text{ nm}, 0.0, 0.0)$$

and

$$\nu_1 = (0.074 \text{ nm}, 1.075 \text{ nm}, 0.0)$$

The shift between neighboring Fe^{II} -centers, caused by interdigitating of the metal centers by the 46.6° tilt angle of the oligomer chains towards the z -axis,⁹ where an Fe^{II} -center within one oligomer chain would fit in-between the Fe^{II} -centers of the neighboring oligomers, was extracted from the atomistic structure as

$$\nu_2' = (1.1076 \text{ nm}, 0.0279 \text{ nm}, 1.0478 \text{ nm}),$$

which translates into a reduced unit cell vector of

$$\nu_2 = (0.8300 \text{ nm}, 0.737 \text{ nm}, 1.0475 \text{ nm})$$

For each redox center, two counter-ions were placed at a shift of $0.5 \times \nu_0$ and $0.5 \times \nu_1$ from the Fe^{II} position, which is in the middle between the Fe^{II} -ions of two neighboring oligomers under the assumption of periodic boundary conditions in the xy -plane.

To account for Pauli repulsion, a weak Lennard-Jones potential was included with $\sigma = 5 \text{ \AA}$ and $\varepsilon = 0.25 \text{ kJ mol}^{-1}$. Periodic boundary conditions were then applied in the xy -plane with unit cell vectors ν_0 and ν_1 (periodic boundary conditions along the z -direction were suppressed by setting the box size to 100 nm in z -direction).

The calculation of the TPT-dimer in the gas phase, as shown in Fig. 1, is done at the PBE theory level⁴⁰ employing a double numerical basis set including polarization functions (DNP) as implemented in Dmol³ (Accelrys, San Diego).

Conflicts of interest

There are no conflicts to declare.

Acknowledgements

V. M., W. W., and F. v. W. acknowledge funding from the EU project MMM@HPC, furthermore, V. M. and W. W. acknowledge support of ERA-NET project MODIGLIANI.

References

- 1 T. W. Kim, G. N. Wang, H. Lee and T. Lee, Statistical analysis of electronic properties of alkanethiols in metal-molecule-metal junctions, *Nanotechnology*, 2007, **18**, 31.
- 2 H. Haick, J. Ghabboun and D. Cahen, Pd versus Au as evaporated metal contacts to molecules, *Appl. Phys. Lett.*, 2005, **86**, 042113.
- 3 H. B. Akkerman, P. W. M. Blom, D. M. de Leeuw and B. de Boer, Towards molecular electronics with large-area molecular junctions, *Nature*, 2006, **441**, 69–72.
- 4 T. Li, J. R. Hauptmann, Z. Wei, S. Petersen, N. Bovet, T. Vosch, J. Nygard, W. Hu, Y. Liu, T. Bjornholm, K. Nygaard and B. W. Laursen, Solution-Processed Ultrathin Chemically Derived Graphene Films as Soft Top Contacts for Solid-State Molecular Electronic Junctions, *Adv. Mater.*, 2012, **24**(10), 1333–1339.
- 5 R. C. Chiechi, E. A. Weiss, M. D. Dickey and G. M. Whitesides, Eutectic gallium-indium (EGaIn): A moldable liquid metal for electrical characterization of self-assembled monolayers, *Angew. Chem., Int. Ed.*, 2008, **47**(1), 142–144.
- 6 M. J. Preiner and N. A. Melosh, Creating large area molecular electronic junctions using atomic layer deposition, *Appl. Phys. Lett.*, 2008, **92**(21), 213301.
- 7 A. J. Bergren, K. D. Harris, F. J. Deng and R. L. McCreery, Molecular electronics using diazonium-derived adlayers on carbon with Cu top contacts: critical analysis of metal oxides and filaments, *J. Phys.: Condens. Matter*, 2008, **20**, 37.
- 8 A. Morteza Najarian, B. Szeto, U. M. Tefashe and R. L. McCreery, Robust All-Carbon Molecular Junctions on Flexible or Semi-Transparent Substrates Using Process-Friendly Fabrication, *ACS Nano*, 2016, **10**(9), 8918–8928.
- 9 Z. Karipidou, B. Branchi, M. Sarpasan, N. Knorr, V. Rodin, P. Friederich, T. Neumann, V. Meded, S. Rosselli, G. Nelles, W. Wenzel, M. A. Rampi and F. von Wrochem, Ultrarobust Thin-Film Devices from Self-Assembled Metal-Terpyridine Oligomers, *Adv. Mater.*, 2016, **28**(18), 3473–3480.
- 10 N. Tuccitto, V. Ferri, M. Cavazzini, S. Quici, G. Zhavnerko, A. Licciardello and M. A. Rampi, Highly conductive similar to 40-nm-long molecular wires assembled by stepwise incorporation of metal centres, *Nat. Mater.*, 2009, **8**(1), 41–46.
- 11 M. Maskus and H. D. Abruna, Synthesis and Characterization of Redox-Active Metal Complexes Sequentially Self-Assembled onto Gold Electrodes via a New Thiol-Terpyridine Ligand, *Langmuir*, 1996, **12**(18), 4455–4462.
- 12 A. Auditore, N. Tuccitto, G. Marzanni, S. Quici, F. Puntoriero, S. Campagna and A. Licciardello, Organized assemblies of thiol-terpyridine and thiophenol on gold surfaces: preferential composition of mixed species evidenced, *Chem. Commun.*, 2003, (19), 2494–2495.
- 13 A. Winter, S. Hoepfener, G. R. Newkome and U. S. Schubert, Terpyridine-Functionalized Surfaces: Redox-Active, Switchable, and Electroactive Nanoarchitectures, *Adv. Mater.*, 2011, **23**(31), 3484–3498.
- 14 N. Tuccitto, I. Delfanti, V. Torrisi, F. Scandola, C. Chiorboli, V. Stepanenko, F. Wurthner and A. Licciardello, Supramolecular self-assembled multilayers of terpyridine-functionalized perylene bisimide metal complexes, *Phys. Chem. Chem. Phys.*, 2009, **11**(20), 4033–4038.
- 15 T. Kurita, Y. Nishimori, F. Toshimitsu, S. Muratsugu, S. Kume and H. Nishihara, Surface Junction Effects on the Electron Conduction of Molecular Wires, *J. Am. Chem. Soc.*, 2010, **132**(13), 4524–4525.

- 16 C. Musumeci, G. Zappalá, N. Martsinovich, E. Orgiu, S. Schuster, S. Quici, M. Zharnikov, A. Troisi, A. Licciardello and P. Samori, Nanoscale Electrical Investigation of Layer-by-Layer Grown Molecular Wires, *Adv. Mater.*, 2014, **26**(11), 1688–1693.
- 17 K. i. Terada, H. Nakamura, K. Kanaizuka, M. a. Haga, Y. Asai and T. Ishida, Long-Range Electron Transport of Ruthenium-Centered Multilayer Films via a Stepping-Stone Mechanism, *ACS Nano*, 2012, **6**(3), 1988–1999.
- 18 B. D. Booth, S. G. Vilt, J. B. Lewis, J. L. Rivera, E. A. Buehler, C. McCabe and G. K. Jennings, Tribological Durability of Silane Monolayers on Silicon, *Langmuir*, 2011, **27**(10), 5909–5917.
- 19 N. Tuccitto, V. Torrisi, M. Cavazzini, T. Morotti, F. Puntoriero, S. Quici, S. Campagna and A. Licciardello, Stepwise Formation of Ruthenium(II) Complexes by Direct Reaction on Organized Assemblies of Thiol-Terpyridine Species on Gold, *ChemPhysChem*, 2007, **8**(2), 227–230.
- 20 R. Sakamoto, S. Katagiri, H. Maeda and H. Nishihara, Bis(terpyridine) metal complex wires: Excellent long-range electron transfer ability and controllable intrawire redox conduction on silicon electrode, *Coord. Chem. Rev.*, 2013, **257**(9–10), 1493–1506.
- 21 R. Berger, Y. Cheng, R. Förch, B. Gotsmann, J. S. Gutmann, T. Pakula, U. Rietzler, W. Schärfl, M. Schmidt, A. Strack, J. Windeln and H. J. Butt, Nanowear on Polymer Films of Different Architecture, *Langmuir*, 2007, **23**(6), 3150–3156.
- 22 S. Hassani, Z. Sobat and H. R. Aghabozorg, Force nanolithography on various surfaces by atomic force microscope, *Int. J. Nanomanuf.*, 2010, **5**(3-4), 217–224.
- 23 R. Kaneko and E. Hamada, Microwear processes of polymer surfaces, *Wear*, 1993, **162**, 370–377.
- 24 R. H. Schmidt, G. Haugstad and W. L. Gladfelter, Scan-Induced Patterning in Glassy Polymer Films: Using Scanning Force Microscopy To Study Plastic Deformation at the Nanometer Length Scale, *Langmuir*, 2003, **19**(3), 898–909.
- 25 G. F. Meyers, B. M. DeKoven and J. T. Seitz, Is the molecular surface of polystyrene really glassy?, *Langmuir*, 1992, **8**(9), 2330–2335.
- 26 J. D. Gale and A. L. Rohl, The General Utility Lattice Program (GULP), *Mol. Simul.*, 2003, **29**(5), 291–341.
- 27 G. J. O. Beran, Modeling Polymorphic Molecular Crystals with Electronic Structure Theory, *Chem. Rev.*, 2016, **116**(9), 5567–5613.
- 28 J. Hoja, A. M. Reilly and A. Tkatchenko, First-principles modeling of molecular crystals: structures and stabilities, temperature and pressure, *Wiley Interdiscip. Rev.: Comput. Mol. Sci.*, 2017, **7**(1), e1294.
- 29 S. Feng and T. Li, Predicting Lattice Energy of Organic Crystals by Density Functional Theory with Empirically Corrected Dispersion Energy, *J. Chem. Theory Comput.*, 2006, **2**(1), 149–156.
- 30 O. Treutler and R. Ahlrichs, Efficient molecular numerical integration schemes, *J. Chem. Phys.*, 1995, **102**(1), 346–354.
- 31 A. Schäfer, H. Horn and R. Ahlrichs, Fully optimized contracted Gaussian basis sets for atoms Li to Kr, *J. Chem. Phys.*, 1992, **97**(4), 2571–2577.
- 32 A. D. Becke, Density-functional exchange-energy approximation with correct asymptotic behavior, *Phys. Rev. A: At., Mol., Opt. Phys.*, 1988, **38**, 3098–3100.
- 33 J. P. Perdew, Density-functional approximation for the correlation energy of the inhomogeneous electron gas, *Phys. Rev. B: Condens. Matter Mater. Phys.*, 1986, **33**, 8822–8824.
- 34 S. Grimme, Semiempirical GGA-type density functional constructed with a long-range dispersion correction, *J. Comput. Chem.*, 2006, **27**(15), 1787–1799.
- 35 P. Eastman, M. S. Friedrichs, J. D. Chodera, R. J. Radmer, C. M. Bruns, J. P. Ku, K. A. Beauchamp, T. J. Lane, L. P. Wang, D. Shukla, T. Tye, M. Houston, T. Stich, C. Klein, M. R. Shirts and V. S. Pande, OpenMM 4: A Reusable, Extensible, Hardware Independent Library for High Performance Molecular Simulation, *J. Chem. Theory Comput.*, 2013, **9**(1), 461–469.
- 36 P. Eastman and V. S. Pande, OpenMM: A Hardware-Independent Framework for Molecular Simulations, *Comput. Sci. Eng.*, 2010, **12**(4), 34–39.
- 37 J. A. Majewski and P. Vogl, Crystal Stability and Structural Transition Pressures of sp-Bonded Solids, *Phys. Rev. Lett.*, 1986, **57**(11), 1366–1369.
- 38 D. Nabok, P. Puschnig and C. Ambrosch-Draxl, Cohesive and surface energies of pi-conjugated organic molecular crystals: A first-principles study, *Phys. Rev. B: Condens. Matter Mater. Phys.*, 2008, **77**(24), 245316.
- 39 J. E. Beves, P. Chwalisz, E. C. Constable, C. E. Housecroft, M. Neuburger, S. Schaffner and J. A. Zampese, A new polymorph of 4'-tolyl-2,2':6',2''-terpyridine (ttpy) and the single crystal structures of [Fe(tpy)₂][PF₆]₂ and [Ru(tpy)₂][PF₆]₂, *Inorg. Chem. Commun.*, 2008, **11**(9), 1009–1011.
- 40 J. P. Perdew, K. Burke and M. Ernzerhof, Generalized Gradient Approximation Made Simple, *Phys. Rev. Lett.*, 1996, **77**, 3865–3868.